Colloids and Surfaces B: Biointerfaces 182 (2019) 110338

Contents lists available at ScienceDirect

Colloids and Surfaces B: Biointerfaces

journal homepage: www.elsevier.com/locate/colsurfb

Quantitative accounting of dye leakage and photobleaching in single lipid vesicle measurements: Implications for biomacromolecular interaction analysis

Soohyun Park[a], Joshua A. Jackman[b], Nam-Joon Cho[a,c,*]

[a] School of Materials Science and Engineering, Nanyang Technological University, 50 Nanyang Avenue 639798, Singapore
[b] School of Chemical Engineering, Sungkyunkwan University, Suwon 16419, Republic of Korea
[c] School of Chemical and Biomedical Engineering, Nanyang Technological University, 62 Nanyang Drive 637459, Singapore

ARTICLE INFO

Keywords:
Lipid vesicles
Membrane-active peptide
Fluorescence microscopy
Surface functionalization
Biomacromolecular interactions

ABSTRACT

Highly parallel measurements on single, tethered lipid vesicles enable real-time monitoring of dynamic membrane interactions of relevance to medical, pharmaceutical, and biotechnological applications. Monitoring the time-dependent release of entrapped fluorescent dyes is a popular measurement approach, although it is often challenging to accurately extract quantitative biochemical parameters. Key issues include dye leakage and imaging-related photobleaching, and corrective measures are needed. Herein, we present an extended analytical framework to collect and interpret time-lapsed fluorescence microscopy imaging data, and demonstrate its utility for tracking membrane-peptide interactions. Our approach is focused on improving platform design and data analysis. First, we identified suitable membrane compositions to minimize dye leakage while enhancing the biomimetic character of lipid vesicles. Second, a data normalization procedure was developed to correct for experimental artifacts, namely dye leakage and photobleaching, and hence improve measurement accuracy. This analytical procedure was applied to experimentally determine the rate of peptide-induced pore formation in single lipid vesicles, and there was up to a nearly three-fold decrease in the measured rate, as compared to uncorrected data. Taken together, the results present a broadly applicable analytical framework to account for experimental artifacts and improve measurement accuracy in highly parallel, single lipid vesicle arrays.

1. Introduction

The rational design of nanoscopic soft matter assemblies at solid-liquid interfaces offers excellent potential for developing nanoarchitectonic-based measurement platforms for a wide range of biosensing and biotechnology applications [1–4]. Towards this goal, surface-based model membranes are useful experimental platforms for characterizing dynamic membrane interactions involving biomacromolecules such as interfacial enzymes and amphipathic peptides [5,6]. There are many different types of model membrane platforms, including supported lipid bilayers [7], tethered lipid bilayers [8], and adsorbed/tethered vesicles [9], that mimic key features of biological membranes. Depending on the application, different model membranes have particular sensing merits and adsorbed/tethered lipid vesicles have provided a versatile model system to interrogate the mechanism of action of membrane-active compounds [10–12].

In some cases, lipid vesicles adsorb via physisorption onto a solid support and form a close-packed layer [13]. Membrane-active compounds are then added to the adsorbed vesicle layer and numerous surface-sensitive techniques can be utilized to study interaction processes, including acoustic [14] and optical [15] sensors. These approaches focus on measuring time-resolved changes in adlayer properties such as film mass, leading to insights into membrane curvature [16], lipid composition [17], and membrane swelling [18]. However, data interpretation is oftentimes challenging because the measurements are conducted on the ensemble-level and influenced by vesicle-substrate and vesicle-vesicle interactions [19]. Hence, there is strong interest in developing surface-based lipid vesicle platforms that enable direct investigation of biomacromolecular interactions at the single-vesicle level [20–22].

Towards this goal, the tethering of sub-100 nm lipid vesicles offers excellent potential to prepare surface-based lipid vesicle platforms. The surface is oftentimes functionalized with a passivating layer such that nonspecific vesicle adsorption is nullified while specific tethering of

* Corresponding author at: School of Materials Science and Engineering, Nanyang Technological University, 50 Nanyang Avenue 639798, Singapore.
E-mail address: njcho@ntu.edu.sg (N.-J. Cho).

https://doi.org/10.1016/j.colsurfb.2019.06.067
Received 14 April 2019; Received in revised form 8 June 2019; Accepted 28 June 2019
Available online 30 June 2019

lipid vesicles is aided by high-affinity noncovalent interactions such as biotin-streptavidin [23], nucleic acid hybridization [24], and alkyl chain attachment [25]. The platforms can be tracked using fluorescence microscopy techniques, including confocal [26,27], total internal reflection [28,29] and epifluorescence [30] modes, or alternatively label-free methods such as interferometric [31] and evanescent [32] light-scattering microscopy techniques. In such embodiments, individual vesicles are detected on the basis of fluorescent labels or light scattering properties [33,34]. Importantly, time-lapsed imaging capabilities enable highly parallel measurements across thousands of individual lipid vesicles in a single experiment [35].

Since dynamic membrane interactions often involve steps such as membrane permeabilization and membrane lysis, there has been interest in developing multi-probe systems whereby individual measurement responses are sensitive to different aspects of interaction processes. For example, a two-fluorophore approach for single-vesicle measurements has been described [28,36] that incorporates water-soluble calcein in the vesicle interior and a rhodamine-labeled phospholipid in the vesicle's lipid bilayer. In general, a key premise is that the fluorescence signals are stable in the absence of an added membrane-active compound. However, numerous experimental factors can affect the fluorescence signals, including photobleaching and dye leakage [37,38]. As a result, there is an outstanding need to improve measurement accuracy by improving platform design along with establishing normalization procedures to correct for experimental artifacts.

Herein, we present an extended analytical framework to collect and interpret time-lapsed fluorescence microscopy imaging data and demonstrate its applicability for accurately measuring the rate of peptide-induced pore formation in single lipid vesicles. Systematic experiments identified that dye leakage and imaging-related photobleaching cause experimental artifacts, leading us to employ more stable lipid compositions and develop a data normalization procedure to correct for experimental artifacts.

2. Materials and methods

2.1. Reagents

Lipids, including 1,2-dioleoyl-*sn*-glycero-3-phosphocholine (DOPC), 1,2-dioleoyl-*sn*-glycero-3-phospho-L-serine (DOPS), 1,2-distearoyl-*sn*-glycero-3-phosphoethanolamine-N-[biotinyl(polyethylene glycol)-2000] (DSPE-PEG(2000)biotin), and 1,2-dioleoyl-*sn*-glycero-3-phosphoethanolamine-N-(lissamine rhodamine B sulfonyl) (Rh-PE), along with cholesterol (ovine wool) were obtained from Avanti Polar Lipids (Alabaster, AL, USA), and received in chloroform stock solutions. An amphipathic, α-helical (AH) peptide (SGSWLRDVWDWICTVLTDFKT-WLQSKL-NH_2) was synthesized by Anaspec Corporation (Fremont, CA, USA) and supplied in lyophilized form. A stock solution was prepared by dissolving AH peptide in deionized water, and the molar concentration of peptide was determined by absorbance measurements at 280 nm wavelength. All dilution steps were performed using 10 mM Tris [pH 7.5] buffer solution with 150 mM NaCl (experimental buffer). All solutions were prepared using high-purity, Milli-Q-treated water (MilliporeSigma, Burlington, MA, USA).

2.2. Vesicle preparation

Small unilamellar vesicles (SUVs) were prepared by the extrusion method, as previously described [39]. The phospholipid/sterol mixture (DOPC alone or with DOPS or cholesterol) included 0.7 mol % of Rh-PE (maximum excitation and emission wavelengths of 560 and 583 nm, respectively) and 0.1 mol % DSPE-PEG(2000)biotin, and all components were dissolved and mixed in chloroform, and then dried under a stream of nitrogen air. Afterwards, the dried lipid film was incubated overnight under vacuum to remove residual chloroform. Multilamellar vesicles were then generated by hydrating and vortexing the lipid sample in a 10 mM Tris [pH 7.5] buffer solution with 150 mM NaCl at a mass concentration of 2 mg/ml. In the buffer, 14.3 mM calcein dye (maximum excitation and emission properties of 494 and 517 nm, respectively, which is well-suited for tracking applications; see Ref [40].) was included to facilitate dye encapsulation within the lipid vesicles. After hydrating the lipid samples, the vesicles were subjected to seven cycles of freeze-thaw treatment to increase encapsulation efficiency and unilamellarity. Then, the lipid suspension was repeatedly passed through a 100-nm diameter polycarbonate filter for a total of 11 times by using a MiniExtruder (Avanti Polar Lipids). The as-prepared vesicle suspensions were diluted right before experiment to a mass concentration of 0.2 mg/ml, and non-encapsulated calcein was removed by a Sephadex G-25 gel filtration column (GE Healthcare Life Sciences, Pittsburgh, PA, USA) [28].

2.3. Epifluorescence microscopy

Imaging experiments were conducted using a Nikon Eclipse Ti-E inverted microscope with a 60× oil-immersion objective (NA 1.49). The excitation source was a mercury-fiber illuminator C-HGFIE Intensilight (Nikon, Tokyo, Japan), and the light was passed through an alternating dichroic filter block (Ex 480/40, Em 535/50) or (Ex 545/30, Em 605/70) for imaging in the FITC and TRITC channels, respectively. An Andor iXon3 897 EMCCD camera was used to obtain the images at the rate of 1 frame per 0.4, 1 or 15 min in 4, 8 or 12 neighboring spots, respectively, to minimize thermal drift and loss of focus. The experimental substrate was enclosed within a microfluidic chamber, and liquid sample was introduced at a flow rate of 100 μl/min, as controlled by a peristaltic pump (model no. ISM833C, Ismatec, Wertheim, Germany).

2.4. Tethered vesicle platform

Glass coverslips (ibidi GmbH, Martinsried, Germany) were cleaned and treated with oxygen plasma (model no. PDC-002, Harrick Plasma, Ithaca, NY, USA) for 30 s, before being assembled in a microfluidic chamber (sticky slide VI 0.4, ibidi GmbH). The coverslips were then coated with a mixture of 50/50 wt% poly(L-lysine)-grafted poly(ethylene glycol) (PLL-g-PEG) and poly(L-lysine)-grafted poly(ethylene glycol)-biotin (PLL-g-PEG-biotin) (SuSoS AG, Dübendorf, Switzerland) at a bulk mass concentration of 41.5 μg/ml. The incubation time was 30 min followed by rinsing in equivalent buffer solution. Then, the surface was incubated with 10 μg/ml neutravidin for 5 min, followed by buffer washing. Biotinylated vesicles were next immobilized on the functionalized surface by biotin-neutravidin coupling at a bulk mass concentration of 0.025 μg/ml. All materials were introduced at a flow rate of 100 μl/min by using a peristaltic pump (Ismatec).

2.5. Image analysis

The single vesicle image analysis was performed using ImageJ software (National Institutes of Health, Bethesda, MD) and an in-house software program written in Python code, as previously described [28,41]. The process is divided into three steps: image adjustment; extraction of fluorescence intensity for individual vesicles; and exponential decay fit to acquire histograms. Image adjustment comprises background removal and image alignment, which is achieved by applying least-squares fits to remove background noise and minimize residual errors across the entire time series. Then, the fluorescence intensity of individual vesicles was extracted by labeling all vesicles that were above a defined threshold value. As described in Ref [30], defining the threshold is an important step for analyzing the correlation between vesicle size and fluorescence intensity. As a result, the time-resolved data reporting the change in an individual vesicle's fluorescence intensity was exported and fit using a nonlinear (exponential decay) function to obtain the onset of pore formation (as indicated by

the calcein signal) or rupture time (as indicated by the rhodamine signal) during the vesicle rupture process.

2.6. Statistical analysis

To compare results between adjacent test groups, the two-tailed *t*-test was performed in order to calculate p-values ($^{*}P < 0.05$, $^{***}P < 0.001$). In the box plots, the boundary of the box closest to zero indicates the 25th percentile, a black line within the box marks the median, a circle symbol within the box marks the mean, and the boundary of the box farthest from zero indicates the 75th percentile. Whiskers below and above the box indicate the 5th and 95th percentiles, respectively. The number of vesicles analyzed per sample was typically > 500 and the standard deviation (s.d.) was defined as IQR/1.35, where IQR is the interquartile range. For histogram plots, the mean ± s.d. was determined by Gaussian fitting and s.d. is defined as FWHM/2.355, where FWHM is the full-width-at-half-maximum.

3. Results and discussion

3.1. Highly parallel measurement platform for single vesicle analysis

As part of the platform, fluorescently labeled vesicles were tethered to a thin layer of PLL-g-PEG-biotin coating by biotin-neutravidin-biotin coupling (Fig. 1A) [42]. Vesicles were immobilized at low surface coverage, which enables high spatial discrimination between individual vesicles for monitoring purposes (Fig. 1B). Up to ˜300 vesicles are observed per field of view and highly parallel measurements are attainable by scanning multiple fields of view in coordinated fashion (Fig. S1). The tethered vesicles contained two different fluorescent labels for probing membrane interaction processes. Water-soluble calcein was included in the vesicle interior and a decrease in the calcein signal indicated membrane permeabilization (pore formation) [43], while rhodamine-labeled phospholipids were included in the lipid bilayer and a decrease in the rhodamine signal signified membrane lysis [44].

3.2. Quantification of photobleaching effect on single lipid vesicles

Photobleaching involves the photochemical destruction of fluorophores, and is a cumulative effect that arises from repeated excitation-emission cycles and depends on numerous factors, including dye properties along with exposure frequency, exposure time and excitation energy (light intensity) [45]. In experiments, the frequency of light exposure, which is defined as the imaging (time) interval, is an important parameter to optimize. Therefore, we sought to quantify the effects of different imaging time intervals on the fluorescence properties of single vesicles. During imaging, blue (494 nm) and green (560 nm) fluorescent light were used to excite calcein and rhodamine dyes for 20 and 100 ms, respectively, followed by detection of green or red emitted light at the longer wavelengths of 517 nm (calcein) and 583 nm (rhodamine), respectively (Fig. 2A). We first checked the stability of the two fluorescence signals associated with individual vesicles under ambient conditions (buffer flow) for 60 min. Image collection was conducted every 0.4, 1, or 15 min. The 3D contour plots of the fluorescence intensity profile for a representative vesicle show how the calcein signal typically decreased over time, while the rhodamine signal remained largely stable (Fig. 2B). In addition, excitation with shorter-wavelength light (*i.e.*, blue light as compared to green light) typically causes greater photobleaching effects as well [46].

Representative changes in the calcein signal for individual vesicles as a function of imaging interval (0.4, 1, and 15 min) are presented in Fig. 2C. With increasing frequency of light exposure (shorter imaging interval), the intensity of the calcein signal decreased more quickly and to a greater extent. For each tested imaging interval, > 1000 vesicles were monitored in parallel and the calcein intensity for each individual vesicle at the end of the measurement period (at 60 min.) was recorded (Fig. 2D). For the 0.4 and 1-min imaging intervals, the mean calcein signal dropped to 0.15 ± 0.08 and 0.16 ± 0.08, respectively. On the other hand, for the 15-min interval, the mean calcein signal was around 0.50 ± 0.20, indicating that less photobleaching occurred than with the more frequent imaging intervals.

Likewise, the dependence on the imaging interval supports that the drop in calcein signal is related to the photobleaching effect [47]. By contrast, the rhodamine signal for individual vesicles showed minimal changes across the 60-min measurement period for all tested imaging intervals, as presented in Fig. 2E. The mean rhodamine signal for 0.4, 1, 15 min was 0.94 ± 0.04, 0.94 ± 0.04, and 0.95 ± 0.04 respectively (Fig. 2F). As such, the data indicate that the calcein signal is sensitive to photobleaching effects while the rhodamine signal is less sensitive, which agrees well with the relatively high photostability of rhodamine-based dyes [48].

3.3. Optimizing membrane composition

We sought to further investigate how membrane composition affects the calcein signal response. Indeed, calcein can translocate across lipid bilayers without membrane disruption [49], especially when lipid vesicles are in the immobilized state [50]. Therefore, we modified the standard zwitterionic lipid composition so that it is more biologically relevant while also improving the stability of the measurement response, *e.g.*, minimizing the nonspecific leakage of calcein molecules.

3.3.1. Effect of incorporating anionic lipids

In order to minimize calcein leakage, we hypothesized that incorporating negatively charged DOPS lipids would be an effective choice because calcein is an acidic molecule (net charge of –4 at pH 7.5; Ref. [51]). Therefore, we tested the effects of incorporating 0–10 mol % DOPS lipid into lipid vesicles on calcein dye leakage. In all cases, the average vesicle diameter was around 115 nm and the lipid compositions were in the fluid-phase state [52] (see Fig. S2).

Representative kinetic curves of individual vesicles are presented for the calcein signal response as a function of DOPS lipid fraction (Fig. 3A). Up to 7.5 mol % DOPS, the rate of decrease in the calcein signal became smaller with increasing DOPC fraction. The trend supports that DOPS lipid incorporation inhibited dye leakage due to electrostatic repulsion between calcein molecules and the lipid bilayer. Interestingly, however, 7.5 mol % DOPS was more effective than 10 mol % DOPS at preventing dye leakage. This observation is likely due to higher DOPS fractions increasing the molecular surface area per lipid headgroup as the result of lateral deformations in the mixed lipid bilayer [53,54]. Hence, there is a balance between inhibiting calcein leakage by promoting electrostatic repulsion between calcein molecules and the lipid bilayer and maintaining structural packing within the lipid bilayer.

Quantitatively, the incorporation of 2.5 and 5 mol % DOPS lipid led to significant increases in the final fluorescence intensity, with values of 0.34 ± 0.06 and 0.35 ± 0.12, respectively (Fig. 3B). Notably, for the 7.5 mol % DOPS, the final fluorescence intensity decreased to only 0.56 ± 0.14, while the final value was 0.37 ± 0.09 for the 10 mol % DOPS case. Altogether, the results support that incorporation of DOPS lipid into tethered vesicles can mitigate nonspecific release of calcein dye, and a specific fraction (7.5 mol % DOPS) improved stability of the calcein signal by over 3-fold. The lipid composition was fixed at a 7.5 mol % DOPS fraction for further testing.

3.3.2. Effect of incorporating cholesterol

We next investigated the effect of incorporating cholesterol into DOPC/DOPS lipid vesicles. Cholesterol is a small amphipathic molecule that intercalates within lipid bilayers and regulates membrane fluidity and rigidity, thereby decreasing membrane permeability [55,56]. Within the test range of cholesterol fractions (0–7.5 mol %), the average vesicle diameters were in the range of 115–120 nm with a slight

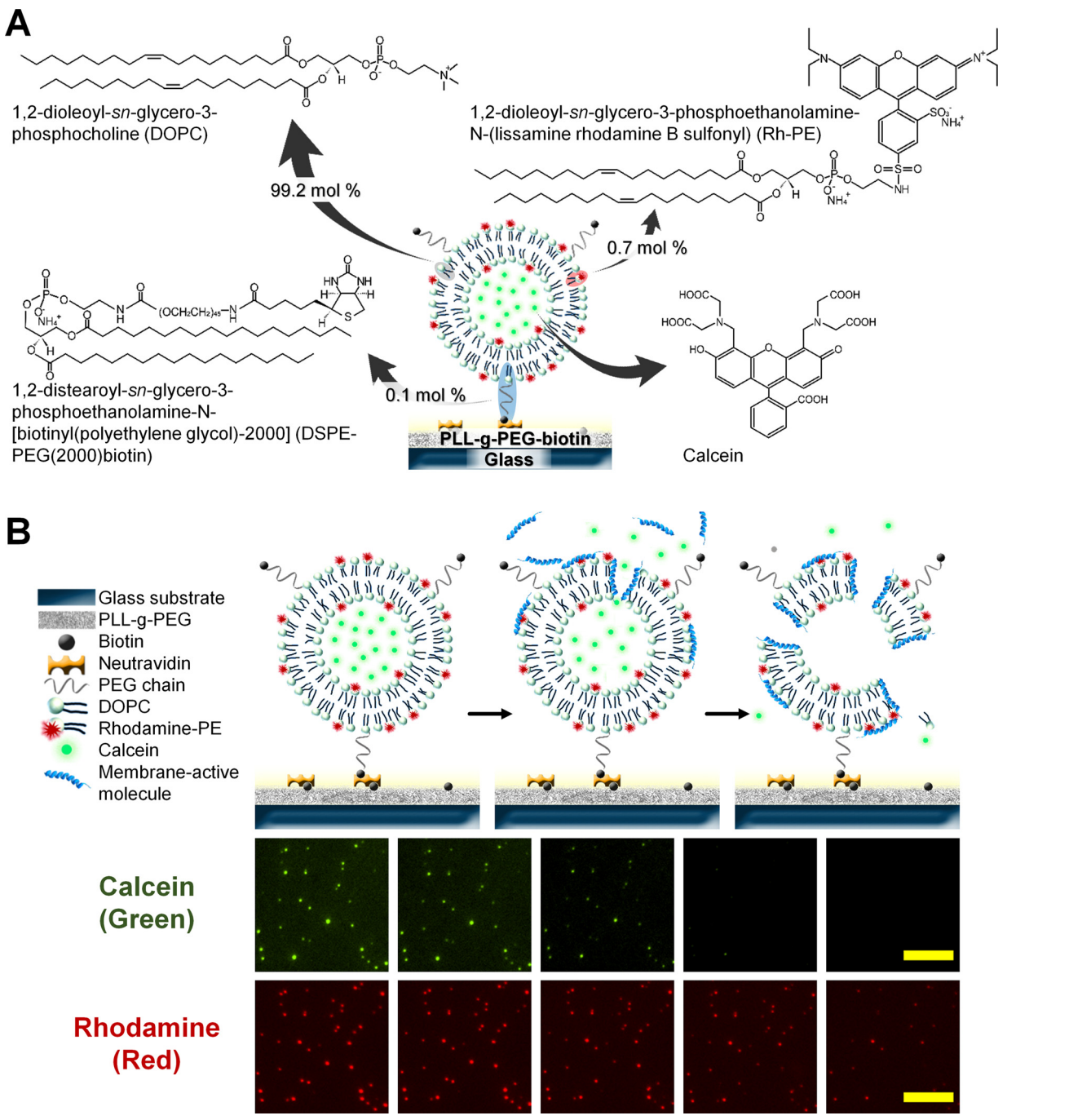

Fig. 1. Schematic illustration of two-probe, highly parallel measurement platform for single vesicle analysis. (A) Molecular structures of the lipid and fluorophore components that are used for constructing the tethered vesicle platform. (B) Top: Schematic illustration of tethered vesicle array for monitoring changes in membrane permeability (water-soluble calcein dye, green; encapsulated within lipid vesicles) and membrane rupture (rhodamine dye-labeled phospholipid, red; in a vesicle's lipid bilayer). Bottom: Time-lapsed imaging is performed, and changes in fluorescence properties of individual, sub-100 nm vesicles can be analyzed. Scale bars are 15 μm.

increase in diameter depending on the cholesterol fraction [55] (see Fig. S2), and the cholesterol-containing membranes can have a coexistence of liquid-disordered and liquid-ordered phases [57,58].

Representative kinetic curves of individual vesicles are presented for the calcein signal response as a function of cholesterol fraction (Fig. 4A). Even small amounts of cholesterol mitigated the nonspecific release of calcein dye, likely due to reinforcing packing between the unsaturated hydrophobic chains of DOPC and DOPS phospholipids within the bilayer [59,60]. At higher cholesterol fractions (5 and 7.5 mol %), there was a similar degree of protection against nonspecific calcein dye release. The results are further corroborated by statistical analysis, indicating that, for 2.5 mol % cholesterol, the mean fluorescence intensity after 60 min was 0.67 ± 0.10, which is significantly higher than the control case without cholesterol (Fig. 4B). Likewise, the mean fluorescence intensity values for 5 and 7.5 mol % cholesterol were 0.71 ± 0.06 and 0.71 ± 0.09, respectively.

Collectively, the results indicate that optimization of the lipid composition, namely by incorporating specific amounts of DOPS lipid and cholesterol, can reduce the extent of nonspecific calcein dye release while maintaining stable rhodamine signals. Of note, similar performance levels were achieved independently of vesicle size, indicating that membrane optimization is a generic approach for stabilizing

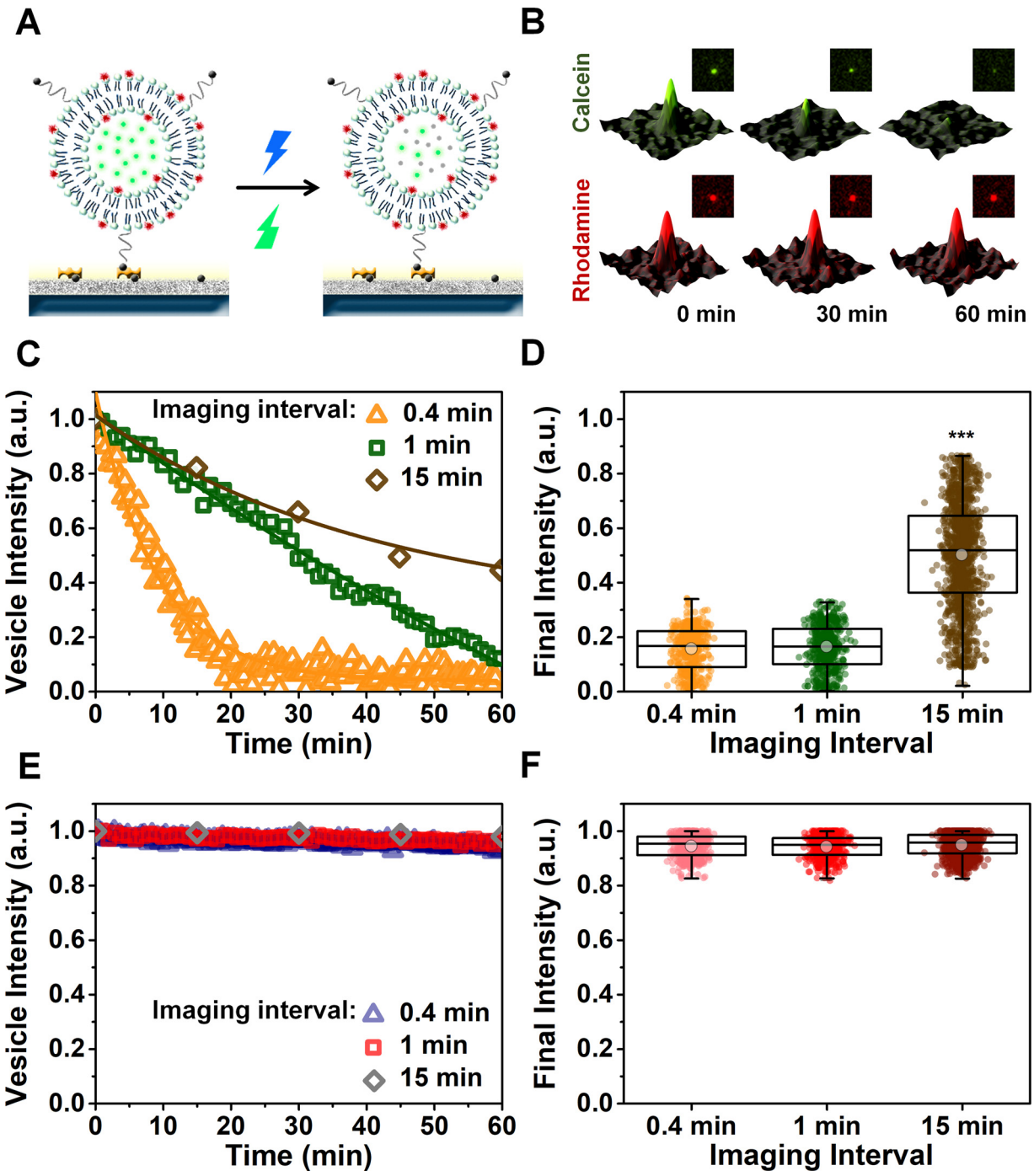

Fig. 2. Time-dependent changes in calcein and rhodamine signals under different imaging interval conditions. (A) Schematic illustration of time-dependent changes in the two measurement signals (B) 3D fluorescence intensity profiles show time-resolved changes in calcein and rhodamine signals. Representative data are shown for a 1-min imaging interval. (C) Time-lapsed changes in the fluorescence intensity of the calcein signal for individual vesicles for different imaging intervals. (D) Statistical comparison of the final intensity of the calcein signal for individual DOPC lipid vesicles at the end of the 60-min measurement period. (E,F) Equivalent data for the rhodamine signal as shown in panels (C,D). $^{***}P < 0.001$ compared to other groups by two-tailed *t*-test.

tethered vesicles (Figs. S3–S4).

3.4. Quantitative evaluation of a membrane-active peptide

Membrane permeabilization and pore formation – processes which are sensitively detected by the release of entrapped calcein dye molecules – are critical steps involved in the mechanism of action of numerous membrane-active compounds such as amphipathic peptides [61]. Artifact-related decreases in the calcein signal can lead to an overestimation of a membrane-active compound's permeabilizing activity. As such, correcting for artifact-related effects can improve measurement accuracy, motivating us to quantitatively evaluate the membrane-disruptive behavior of an amphipathic, α-helical (AH) peptide as a model system [62].

The tested AH peptide is known to form pores in small vesicles (< 160 nm diameter) leading to vesicle rupture once a critical density of pores is formed in the lipid bilayer (Fig. 5A) [63,64]. In single-vesicle measurements, AH peptide-induced pore formation and membrane lysis can be tracked by monitoring time-resolved decreases in the calcein and rhodamine signals, respectively (Fig. 5B). We first investigated the

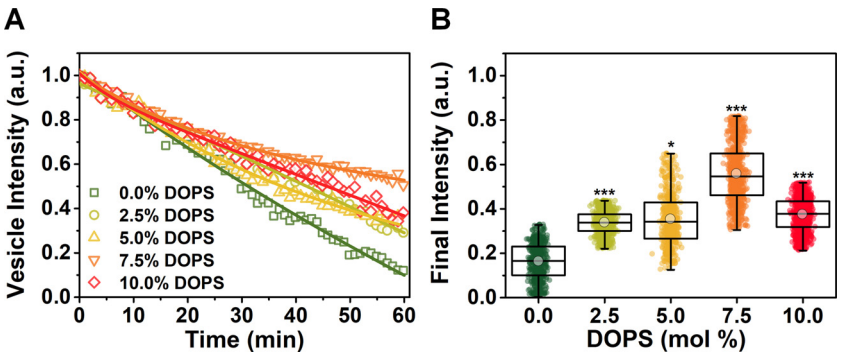

Fig. 3. Influence of DOPS phospholipid incorporation on calcein dye release. (A) Time-lapsed changes in the fluorescence intensity of the calcein signal for individual vesicles as a function of DOPS lipid fraction, with a 1-min imaging interval. (B) Quantification of the normalized fluorescence intensity of individual DOPC/DOPS lipid vesicles after 60 min. Each data point corresponds to a single vesicle. $^{*}P < 0.05$, $^{***}P < 0.001$ compared to other groups by two-tailed *t*-test.

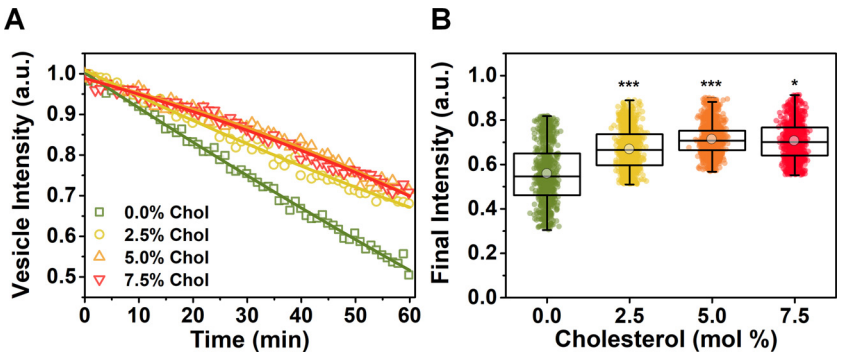

Fig. 4. Influence of cholesterol incorporation on calcein dye release. (A) Time-lapsed changes in the fluorescence intensity of the calcein signal for individual vesicles for different cholesterol fractions, with a 1-min imaging interval. The DOPS lipid fraction was 7.5 mol %. (B) Quantification of the normalized fluorescence intensity of individual DOPC/DOPS lipid vesicles after 60 min. Each data point corresponds to a single vesicle. $^{*}P < 0.05$, $^{***}P < 0.001$ compared to other groups by two-tailed *t*-test.

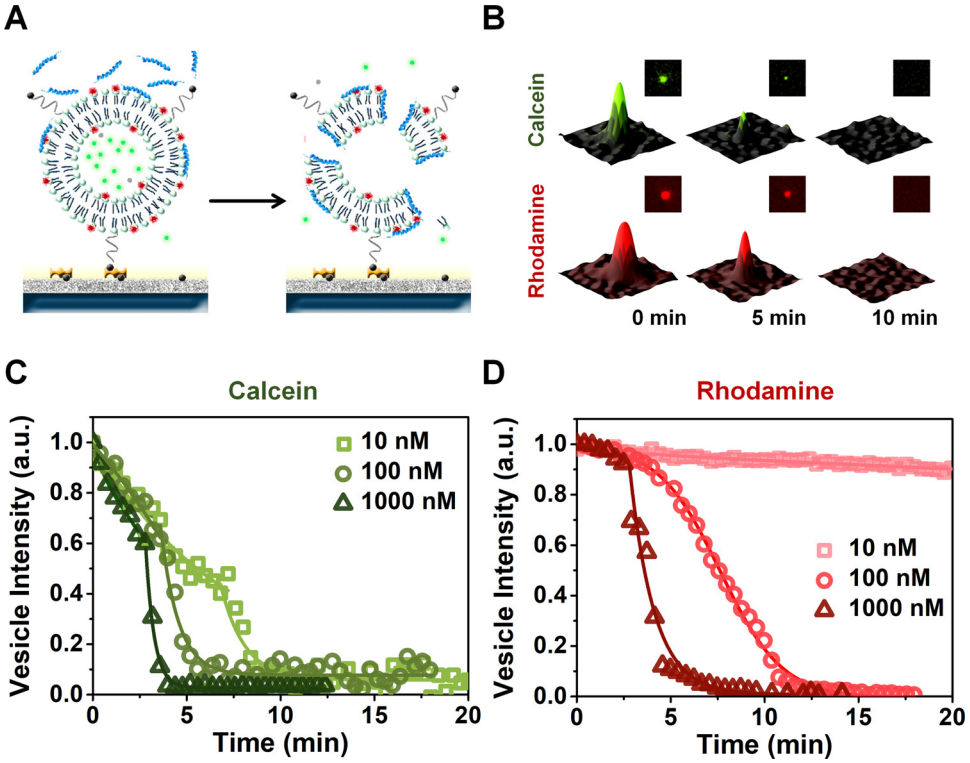

Fig. 5. Single-vesicle tracking of AH peptide-mediated pore formation and vesicle rupture. (A) Schematic illustration of AH peptide-induced pore formation and vesicle rupture. (B) 3D fluorescence intensity profiles show time-resolved changes in calcein and rhodamine signals caused by AH peptide. The peptide concentration was 100 nM. Time-lapsed changes in the fluorescence intensity of the (C) calcein and (D) rhodamine signals for individual vesicles that were treated with different AH peptide concentrations, with a 0.4-min imaging interval.

effects of bulk AH peptide concentration (10–1000 nM) on the time scale of peptide-induced pore formation and corresponding membrane lysis in DOPC lipid vesicles. This range of peptide concentrations was selected because it is sufficiently high to induce pore-induced vesicle rupture while the resulting interaction process occurs on a suitable timescale to track the corresponding interaction kinetics [28,65]. For all tested peptide concentrations, there was a two-step decrease in the calcein signal, namely a nearly linear, gradual decrease followed by a more rapid drop (Fig. 5C). The initial stage coincides with the onset of pore formation in a lipid vesicle and there is hindered diffusion of dye molecules through one or a few pores, while a more rapid drop began after a critical density of pores was formed in the vesicle and more extensive dye release can thus occur until no dye remains inside the vesicle [28,64]. With increasing peptide concentration from 10 nM to 1000 nM, the timescale of calcein release decreased from 7.4 ± 1.2 min to 1.9 ± 0.3 min, as determined by Gaussian curve-

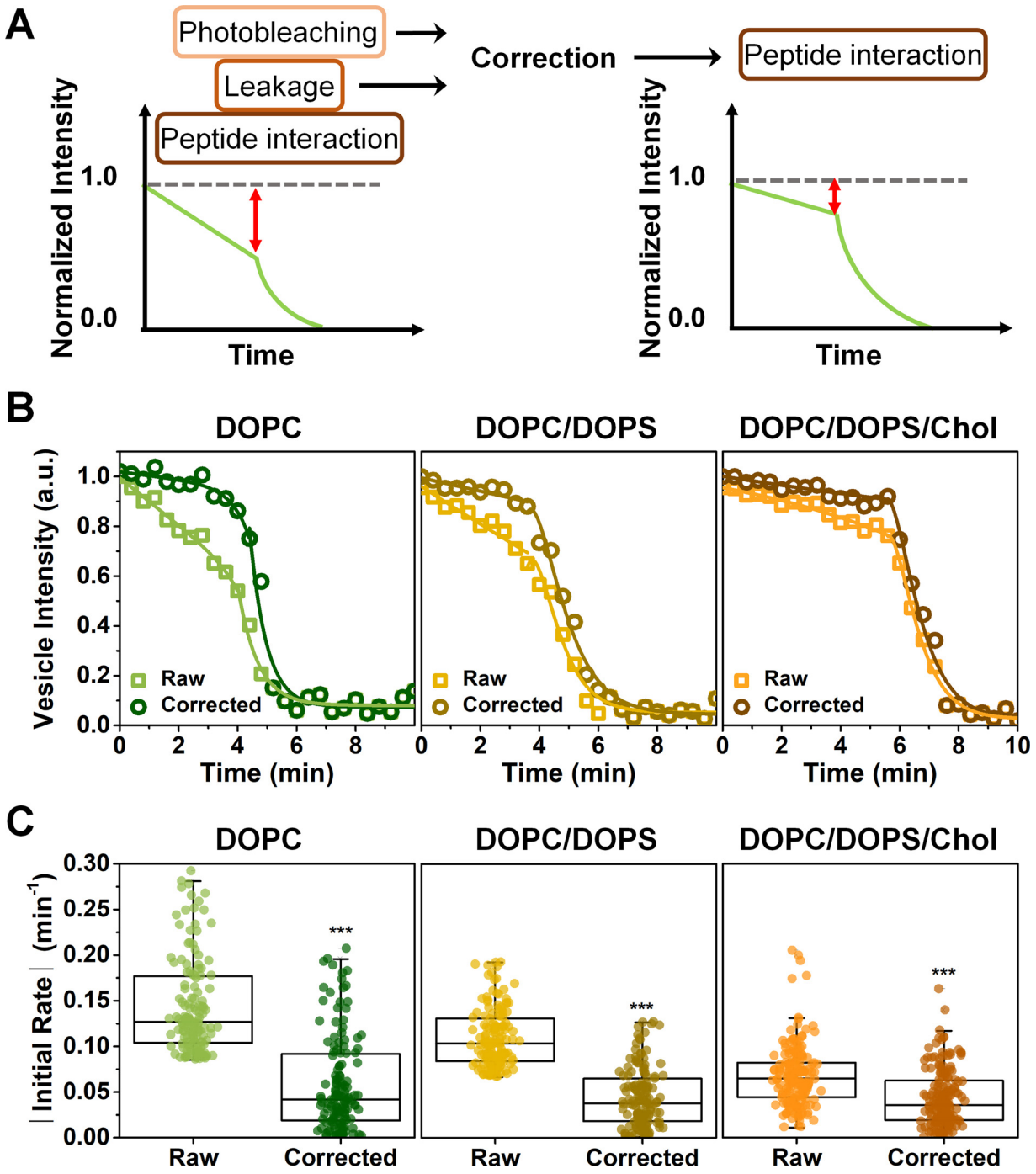

Fig. 6. Corrective measures for single-vesicle analysis of AH peptide-mediated pore formation. (A) Data normalization procedure to correct raw measurement data by removing the effects of dye photobleaching and nonspecific leakage. (B) Time-lapsed changes in the fluorescence intensity of the calcein signal for individual vesicles with different membrane compositions, with a 0.4-min imaging interval. Raw and corrected profiles refer to measurement data before and after normalization procedure is applied. The peptide concentration was 100 nM. (C) Quantification of the initial rate of change in the calcein signal, without and with correction procedure, for individual vesicles with different membrane compositions. Each data point corresponds to a single vesicle. $^{***}P < 0.001$ for the corrected data set compared to the raw data set by two-tailed *t*-test.

fitting analysis of the individual single-vesicle data points plotted in a histogram format (Fig. S5). As further demonstrated by tracking the rhodamine signal, 100 nM and higher concentrations of AH peptide led to eventual vesicle rupture whereas 10 nM AH peptide was ineffective (Fig. 5D). Therefore, we selected 100 nM AH peptide for further experiments because this bulk peptide concentration is sufficiently high to cause pore formation-induced vesicle rupture while the time scale is relatively long and hence quantitative evaluation is encumbered by potential measurement artifacts.

To improve measurement accuracy, we devised a procedure to correct for membrane translocation and photobleaching of calcein molecules (Fig. 6A). Measurement data were collected by tracking the time-resolved changes in calcein signal when 100 nM AH peptide was added to DOPC, DOPC/DOPS, and DOPC/DOPS/cholesterol vesicles (Fig. 6B, reported as raw data). For all membrane compositions, peptide-induced pore formation occurred and the mean times of calcein release were similar for DOPC and DOPC/DOPS vesicles (3.5 ± 1.1 min and 3.6 ± 1.0 min, respectively), while the mean time

increased to 5.8 ± 1.7 min for DOPC/DOPS/cholesterol vesicles (Fig. S6). Under equivalent imaging conditions, we measured the time-resolved change in calcein signal for each membrane composition in the absence of AH peptide and adjusted the experimental data for each membrane composition (Fig. S7). Also, we verified that there was no significant difference in the kinetic data for similar-size vesicles when subtracting the mean values of the time-resolved change in the calcein signal or when subtracting the time-resolved change in the calcein signal corresponding to each individual vesicle (Fig. S8). The corrected AH peptide interaction kinetics (reported as corrected data) indicate that the native measurement response overestimates the rate of change in the initial calcein drop, and the effect is most prominent for DOPC lipid vesicles. The overestimation in the calcein drop is still significant but to a lesser extent for DOPC/DOPS and DOPC/DOPS/cholesterol vesicles.

To quantify the magnitude of the corrective effect for each tested membrane composition, we determined and compared the initial rate of change (slope) in the calcein signal for the raw and corrected kinetic profiles of each individual vesicle (Fig. 6C). The measured slopes provide an indication of the rate of pore formation and hence the degree of membrane-disruptive activity exhibited by AH peptide. For DOPC lipid vesicles, the native measurement response overestimated the rate of pore formation by a 148% relative error (0.14 ± 0.052 vs. 0.058 ± 0.051 min^{-1}), whereas the overestimate had a 58% relative error (0.068 ± 0.034 vs. 0.043 ± 0.030 min^{-1}) in the case of DOPC/DOPS/cholesterol vesicles. Hence, the results indicate that there is up to a three-fold difference in the rate of pore formation depending on the membrane composition and the corrective procedure improves measurement accuracy.

The corrective procedure was also applied to the rhodamine data, although no significant change in the measurement responses was observed (Fig. S9). As mentioned above, this finding is consistent with greater photostability of the rhodamine dye and its phospholipid anchoring ensures that rhodamine molecules remain bound within the lipid bilayer architecture. Taken together, the results demonstrate how the corrective procedure can improve measurement accuracy in cases where the dye probe is susceptible to membrane translocation/leakage and photobleaching effects. In future work, it will interesting to further investigate how these corrective strategies can be applied to improve measurement accuracy for characterizing various types of biomacromolecular interaction processes, especially in cases where membranes exhibit raft-like compositions among other possiblities [66].

4. Conclusion

Our findings demonstrate that experimental artifacts such as dye leakage and imaging-related photobleaching can influence quantitative interpretation of measurement data in single lipid vesicle measurements. By taking into account the physicochemical properties of the tested fluorescent dyes and rationally optimizing the membrane composition, we identified broadly applicable strategies to improve measurement accuracy based on minimizing nonspecific dye leakage and normalizing experimental data to correct for experimental artifacts. The extended analytical framework was applied to accurately measure the rate of peptide-induced pore formation in individual, sub-100 nm lipid vesicles as a model system. Looking forward, these analytical capabilities will prove useful for single lipid vesicle measurements.

Acknowledgments

This work was supported by the National Research Foundation of Singapore through a Competitive Research Programme grant (NRF-CRP10-2012-07) and a Proof-of-Concept grant (NRF2015NRF-POC0001-19) as well as through the Center for Precision Biology at Nanyang Technological University. Additional support was provided by the Creative Materials Discovery Program through the National Research Foundation of Korea funded by the Ministry of Science, ICT and Future Planning (NRF-2016M3D1A1024098). The authors thank Dr. Seyed R. Tabaei for technical training and assistance.

Appendix A. Supplementary data

Supplementary material related to this article can be found, in the online version, at doi:https://doi.org/10.1016/j.colsurfb.2019.06.067.

References

[1] M. Komiyama, K. Yoshimoto, M. Sisido, K. Ariga, Chemistry can make strict and fuzzy controls for bio-systems: DNA nanoarchitectonics and cell-macromolecular nanoarchitectonics, Bull. Chem. Soc. Jpn. 90 (2017) 967–1004.
[2] M. Ramanathan, L.K. Shrestha, T. Mori, Q. Ji, J.P. Hill, K. Ariga, Amphiphile nanoarchitectonics: from basic physical chemistry to advanced applications, Phys. Chem. Chem. Phys. 15 (2013) 10580–10611.
[3] K. Ariga, J. Li, J. Fei, Q. Ji, J.P. Hill, Nanoarchitectonics for dynamic functional materials from atomic-/molecular-level manipulation to macroscopic action, Adv. Mater. 28 (2016) 1251–1286.
[4] K. Ariga, S. Watanabe, T. Mori, J. Takeya, Soft 2D nanoarchitectonics, NPG Asia Mater. (2018) 1.
[5] A. Mashaghi, S. Mashaghi, I. Reviakine, R.M. Heeren, V. Sandoghdar, M. Bonn, Label-free characterization of biomembranes: from structure to dynamics, Chem. Soc. Rev. 43 (2014) 887–900.
[6] T.-H. Lee, D.J. Hirst, K. Kulkarni, M.P. Del Borgo, M.-I. Aguilar, Exploring molecular-biomembrane interactions with surface plasmon resonance and dual polarization interferometry technology: expanding the spotlight onto biomembrane structure, Chem. Rev. 118 (2018) 5392–5487.
[7] M.T. Butko, B. Moree, R.B. Mortensen, J. Salafsky, Detection of ligand-induced conformational changes in oligonucleotides by second-harmonic generation at a supported lipid bilayer interface, Anal. Chem. 88 (2016) 10482–10489.
[8] M. Zhang, Q. Zhai, L. Wan, L. Chen, Y. Peng, C. Deng, J. Xiang, J. Yan, Electrochemical impedance spectroscopy for real-time detection of lipid membrane damage based on a porous self-assembly monolayer support, Anal. Chem. 90 (2018) 7422–7427.
[9] E. Boukobza, A. Sonnenfeld, G. Haran, Immobilization in surface-tethered lipid vesicles as a new tool for single biomolecule spectroscopy, J. Controlled Release 105 (2001) 12165–12170 https://cassi.cas.org/publication.jsp?P=eCQtRPJo9AQyz133K_ll3zLPXfcr-W.
[10] S. Li, P. Hu, N. Malmstadt, Confocal imaging to quantify passive transport across biomimetic lipid membranes, Anal. Chem. 82 (2010) 7766–7771.
[11] P. Kuhn, K. Eyer, S. Allner, D. Lombardi, P.S. Dittrich, A microfluidic vesicle screening platform: monitoring the lipid membrane permeability of tetracyclines, Anal. Chem. 83 (2011) 8877–8885.
[12] K. Eyer, F. Paech, F. Schuler, P. Kuhn, R. Kissner, S. Belli, P.S. Dittrich, S.D. Krämer, A liposomal fluorescence assay to study permeation kinetics of drug-like weak bases across the lipid bilayer, J. Controlled Release 173 (2014) 102–109.
[13] C. Keller, B. Kasemo, Surface specific kinetics of lipid vesicle adsorption measured with a quartz crystal microbalance, Biophys. J. 75 (1998) 1397–1402.
[14] N.-J. Cho, C.W. Frank, B. Kasemo, F. Höök, Quartz crystal microbalance with dissipation monitoring of supported lipid bilayers on various substrates, Nat. Protoc. 5 (2010) 1096–1106.
[15] J.A. Jackman, A.R. Ferhan, N.-J. Cho, Nanoplasmonic sensors for biointerfacial science, Chem. Soc. Rev. 46 (2017) 3615–3660.
[16] N.J. Cho, H. Dvory-Sobol, A. Xiong, S.J. Cho, C.W. Frank, J.S. Glenn, Mechanism of an amphipathic alpha-helical peptide's antiviral activity involves size-dependent virus particle lysis, ACS Chem. Biol. 4 (2009) 1061–1067.
[17] G.J. Hardy, R. Nayak, S. Munir Alam, J.G. Shapter, F. Heinrich, S. Zauscher, Biomimetic supported lipid bilayers with high cholesterol content formed by α-helical peptide-induced vesicle fusion, J. Mater. Chem. 22 (2012) 19506–19513.
[18] N.-J. Cho, G. Wang, M. Edvardsson, J.S. Glenn, F. Hook, C.W. Frank, Alpha-helical peptide-induced vesicle rupture revealing new insight into the vesicle fusion process as monitored in situ by quartz crystal microbalance-dissipation and reflectometry, Anal. Chem. 81 (2009) 4752–4761.
[19] G.H. Zan, N.-J. Cho, Rupture of zwitterionic lipid vesicles by an amphipathic, α-helical peptide: indirect effects of sensor surface and implications for experimental analysis, Colloids Surf. B 121 (2014) 340–346.
[20] S.M. Christensen, D.G. Stamou, Sensing-applications of surface-based single vesicle arrays, Sensors 10 (2010) 11352–11368.
[21] A.L. Christensen, C. Lohr, S.M. Christensen, D. Stamou, Single vesicle biochips for ultra-miniaturized nanoscale fluidics and single molecule bioscience, Lab Chip 13 (2013) 3613–3625.
[22] H. Pick, A.C. Alves, H. Vogel, Single-Vesicle assays using liposomes and cell-derived vesicles: from modeling complex membrane processes to synthetic biology and biomedical applications, Chem. Rev. (2018).
[23] D. Stamou, C. Duschl, E. Delamarche, H. Vogel, Self-assembled microarrays of attoliter molecular vessels, Angew. Chem. 115 (2003) 5738–5741.
[24] C. Yoshina-Ishii, S.G. Boxer, Arrays of mobile tethered vesicles on supported lipid bilayers, J. Am. Chem. Soc. 125 (2003) 3696–3697.
[25] M.B. Dowling, V. Javvaji, G.F. Payne, S.R. Raghavan, Vesicle capture on patterned surfaces coated with amphiphilic biopolymers, Soft Matter 7 (2011) 1219–1226.

[26] E. Elizondo, J. Larsen, N.S. Hatzakis, I. Cabrera, T. Bjørnholm, J. Veciana, D. Stamou, N. Ventosa, Influence of the preparation route on the supramolecular organization of lipids in a vesicular system, J. Am. Chem. Soc. 134 (2012) 1918–1921.
[27] N. Ehrlich, A.L. Christensen, D. Stamou, Fluorescence anisotropy based single liposome assay to measure molecule–membrane interactions, Anal. Chem. 83 (2011) 8169–8176.
[28] S.R. Tabaei, M. Rabe, V.P. Zhdanov, N.-J. Cho, F. Höök, Single vesicle analysis reveals nanoscale membrane curvature selective pore formation in lipid membranes by an antiviral α-helical peptide, Nano Lett. 12 (2012) 5719–5725.
[29] P. Flagmeier, S. De, D.C. Wirthensohn, S.F. Lee, C. Vincke, S. Muyldermans, T.P. Knowles, S. Gandhi, C.M. Dobson, D. Klenerman, Ultrasensitive measurement of Ca2+ influx into lipid vesicles induced by protein aggregates, Angew. Chem., Int. Ed. 56 (2017) 7750–7754.
[30] C. Lohr, A.H. Kunding, V.K. Bhatia, D. Stamou, Constructing size distributions of liposomes from single-object fluorescence measurements, Methods Enzymol. 465 (2009) 143–160.
[31] J. Andrecka, K.M. Spillane, J. Ortega-Arroyo, P. Kukura, Direct observation and control of supported lipid bilayer formation with interferometric scattering microscopy, ACS Nano 7 (2013) 10662–10670.
[32] Br. Agnarsson, A. Lundgren, A. Gunnarsson, M. Rabe, A. Kunze, M. Mapar, L. Simonsson, M. Bally, V.P. Zhdanov, F. Höök, Evanescent light-scattering microscopy for label-free interfacial imaging: from single sub-100 nm vesicles to live cells, ACS Nano 9 (2015) 11849–11862.
[33] A.H. Kunding, M.W. Mortensen, S.M. Christensen, D. Stamou, A fluorescence-based technique to construct size distributions from single-object measurements: application to the extrusion of lipid vesicles, Biophys. J. 95 (2008) 1176–1188.
[34] K.I. Mortensen, C. Tassone, N. Ehrlich, T.L. Andresen, H. Flyvbjerg, How to characterize individual nanosize liposomes with simple self-calibrating fluorescence microscopy, Nano Lett. 18 (2018) 2844–2851.
[35] S.M. Christensen, P.-Y. Bolinger, N.S. Hatzakis, M.W. Mortensen, D. Stamou, Mixing subattolitre volumes in a quantitative and highly parallel manner with soft matter nanofluidics, Nat. Nanotechnol. 7 (2012) 51.
[36] S.R. Tabaei, N.J. Cho, Lamellar sheet exfoliation of single lipid vesicles by a membrane-active peptide, Chem. Comm. 51 (2015) 10272–10275.
[37] R. Godin, H.-W. Liu, L. Smith, G. Cosa, Dye lipophilicity and retention in lipid membranes: implications for single-molecule spectroscopy, Langmuir 30 (2014) 11138–11146.
[38] D. Sezer, T. Oruç, Protonation kinetics compromise liposomal fluorescence assay of membrane permeation, J. Phys. Chem. B 121 (2017) 5218–5227.
[39] R.C. MacDonald, R.I. MacDonald, B.P.M. Menco, K. Takeshita, N.K. Subbarao, L.-r. Hu, Small-volume extrusion apparatus for preparation of large, unilamellar vesicles, Biochim. Biophys. Acta Biomembr. 1061 (1991) 297–303.
[40] S. Hamann, J.F. Kiilgaard, T. Litman, F.J. Alvarez-Leefmans, B.R. Winther, T. Zeuthen, Measurement of cell volume changes by fluorescence self-quenching, J. Fluoresc. 12 (2002) 139–145.
[41] J.A. Jackman, R. Saravanan, Y. Zhang, S.R. Tabaei, N.J. Cho, Correlation between membrane partitioning and functional activity in a single lipid vesicle assay establishes design guidelines for antiviral peptides, Small 11 (2015) 2372–2379.
[42] L. Ruiz-Taylor, T. Martin, F. Zaugg, K. Witte, P. Indermuhle, S. Nock, P. Wagner, Monolayers of derivatized poly (L-lysine)-grafted poly (ethylene glycol) on metal oxides as a class of biomolecular interfaces, Proc. Natl. Acad. Sci. U. S. A. 98 (2001) 852–857.
[43] K. Matsuzaki, S. Yoneyama, K. Miyajima, Pore formation and translocation of melittin, Biophys. J. 73 (1997) 831–838.
[44] A. Pramanik, P. Thyberg, R. Rigler, Molecular interactions of peptides with phospholipid vesicle membranes as studied by fluorescence correlation spectroscopy, Chem. Phys. Lipids 104 (2000) 35–47.
[45] L. Song, E. Hennink, I.T. Young, H.J. Tanke, Photobleaching kinetics of fluorescein in quantitative fluorescence microscopy, Biophys. J. 68 (1995) 2588.
[46] F. Helmchen, W. Denk, Deep tissue two-photon microscopy, Nat. Methods 2 (2005) 932.
[47] T. Cordes, A. Maiser, C. Steinhauer, L. Schermelleh, P. Tinnefeld, Mechanisms and advancement of antifading agents for fluorescence microscopy and single-molecule spectroscopy, Phys. Chem. Chem. Phys. 13 (2011) 6699–6709.
[48] S.A. Soper, H.L. Nutter, R.A. Keller, L.M. Davis, E.B. Shera, The photophysical constants of several fluorescent dyes pertaining to ultrasensitive fluorescence spectroscopy, Photochem. Photobiol. 57 (1993) 972–977.
[49] B. Maherani, E. Arab-Tehrany, A. Kheirolomoom, D. Geny, M. Linder, Calcein release behavior from liposomal bilayer; influence of physicochemical/mechanical/structural properties of lipids, Biochimie 95 (2013) 2018–2033.
[50] T. Shimanouchi, H. Ishii, N. Yoshimoto, H. Umakoshi, R. Kuboi, Calcein permeation across phosphatidylcholine bilayer membrane: effects of membrane fluidity, liposome size, and immobilization, Colloids Surf. B 73 (2009) 156–160.
[51] T. Allen, Calcein as a tool in liposome methodology, Liposome Technol. 3 (1984) 177–182.
[52] E. Hellstrand, E. Sparr, S. Linse, Retardation of Aβ fibril formation by phospholipid vesicles depends on membrane phase behavior, Biophys. J. 98 (2010) 2206–2214.
[53] I. van Uitert, S. Le Gac, A. van den Berg, The influence of different membrane components on the electrical stability of bilayer lipid membranes, Biochim. Biophys. Acta Biomembr. 1798 (2010) 21–31.
[54] J. Pan, X. Cheng, L. Monticelli, F.A. Heberle, N. Kučerka, D.P. Tieleman, J. Katsaras, The molecular structure of a phosphatidylserine bilayer determined by scattering and molecular dynamics simulations, Soft Matter 10 (2014) 3716–3725.
[55] P. Losada-Pérez, M. Khorshid, D. Yongabi, P. Wagner, Effect of cholesterol on the phase behavior of solid-supported lipid vesicle layers, J. Phys. Chem. B 119 (2015) 4985–4992.
[56] F. de Meyer, B. Smit, Effect of cholesterol on the structure of a phospholipid bilayer, Proc. Natl. Acad. Sci. U. S. A. 106 (2009) 3654–3658.
[57] J.H. Ipsen, G. Karlström, O. Mourtisen, H. Wennerström, M. Zuckermann, Phase equilibria in the phosphatidylcholine-cholesterol system, Biochim. Biophys. Acta Biomembr. 905 (1987) 162–172.
[58] P.J. Quinn, C. Wolf, The liquid-ordered phase in membranes, Biochim. Biophys. Acta Biomembr. 1788 (2009) 33–46.
[59] W.-C. Hung, M.-T. Lee, F.-Y. Chen, H.W. Huang, The condensing effect of cholesterol in lipid bilayers, Biophys. J. 92 (2007) 3960–3967.
[60] H. Martinez-Seara, T. Róg, M. Pasenkiewicz-Gierula, I. Vattulainen, M. Karttunen, R. Reigada, Interplay of unsaturated phospholipids and cholesterol in membranes: effect of the double-bond position, Biophys. J. 95 (2008) 3295–3305.
[61] W.C. Wimley, Describing the mechanism of antimicrobial peptide action with the interfacial activity model, ACS Chem. Biol. 5 (2010) 905–917.
[62] J.A. Jackman, E. Linardy, D. Yoo, J. Seo, W.B. Ng, D.J. Klemme, N.J. Wittenberg, S.H. Oh, N.J. Cho, Plasmonic nanohole sensor for capturing single virus-like particles toward virucidal drug evaluation, Small 12 (2016) 1159–1166.
[63] J.A. Jackman, G.H. Zan, V.P. Zhdanov, N.-J. Cho, Rupture of lipid vesicles by a broad-spectrum antiviral peptide: influence of vesicle size, J. Phys. Chem. B 117 (2013) 16117–16128.
[64] J.A. Jackman, H.Z. Goh, V.P. Zhdanov, W. Knoll, N.-J. Cho, Deciphering how pore formation causes strain-induced membrane lysis of lipid vesicles, J. Am. Chem. Soc. 138 (2016) 1406–1413.
[65] J.A. Jackman, V.V. Costa, S. Park, A.L.C. Real, J.H. Park, P.L. Cardozo, A.R. Ferhan, I.G. Olmo, T.P. Moreira, J.L. Bambirra, Therapeutic treatment of Zika virus infection using a brain-penetrating antiviral peptide, Nat. Mater. 17 (2018) 971.
[66] P. Losada-Pérez, M. Khorshid, C. Hermans, T. Robijns, M. Peeters, K. Jiménez-Monroy, L. Truong, P. Wagner, Melittin disruption of raft and non-raft-forming biomimetic membranes: a study by quartz crystal microbalance with dissipation monitoring, Colloids Surf. B 123 (2014) 938–944.